Reconstruction Algorithm for Regions of Interest in γ-Photon Images

MIN YAO, **GANG LV**, **MIN ZHAO**, **RUIPENG GUO**, **JIAN LIU**, (Member, IEEE), **DAWEI ZHEN**, **MING WANG**, **FANG XIONG**, AND **WEI LIU**

College of Automation Engineering, Nanjing University of Aeronautics and Astronautics, Nanjing 211106, China
Nondestructive Detection and Monitoring Technology for High Speed Transportation Facilities, Key Laboratory of Ministry of Industry and Information Technology, Nanjing University of Aeronautics and Astronautics, Nanjing 211106, China

Corresponding author: Min Yao (ym_nuaa@163.com)

ABSTRACT As a nondestructive testing technology, γ-photon imaging shows immense potential in the industrial field. However, the limitations of γ-photon imaging theory and detection technology result in various problems, such as low image resolution and edge blur. The technology is particularly difficult to apply to industrial detection that requires high imaging speed and high resolution. Therefore, this study proposes a reconstruction algorithm for regions of interest (ROI) in γ-photon images. The proposed algorithm is suitable for fast industrial detection and is based on the reconstruction algorithm for sinusoidal graph data, that is, the ordered subset expectation maximization (OSEM) image reconstruction algorithm. It is an improvement of the traditional point-and-line system matrix (SM) model. In the application of the proposed algorithm, the probability weight of a pixel is determined by the solid angle of the crystal bar at both ends of the line of response (LOR) to the pixel it passes through. In this work, the known contour parameters of industrial parts are used to describe the area of nuclide distribution as the ROI. Only the pixels through which the LOR passed in the ROI are counted, and the probability weights of these pixels are calculated to construct the SM. Gaussian filters are added in each iteration to suppress the clutter of scattered noise inside the image. The effectiveness of the algorithm was verified in two model experiments. A closed cavity detection experiment on industrial hydraulic parts was also conducted to compare the image reconstruction effects before and after the improvement. Results showed that the proposed algorithm can effectively improve image resolution and image edge contours. In the tee pipe model experiment and cavity detection experiment on hydraulic parts, the image reconstruction speed increased by more than 6 and 10 times, respectively. Hence, the proposed algorithm provided a feasible solution for quickly obtaining images with clear edges and high resolution under a large aperture detector ring.

INDEX TERMS γ-photon imaging, OSEM, ROI, system matrix, industrial nondestructive testing.

I. INTRODUCTION

Positron emission tomography (PET) is a noninvasive imaging diagnostic technique widely used in clinical practice. It provides metabolic information in vivo by imaging radionuclides injected in vivo [1]–[4]. γ-photon imaging is not extensively studied in the industrial field; however, positron annihilation can produce a reverse emission of a 511 keV γ-photon pair, and γ-photon has strong penetration

(penetration thickness of a 30 mm single crystal aluminum, intensity attenuation of 50%) and electric neutrality and is minimally affected by materials, structures, electromagnetic field, and other factors. Therefore, studying industrial γ-photon imaging technology in combination with prior knowledge of industrial parts is of great significance.

Fig. 1 presents a schematic of the inspection process for industrial parts. A solvent labeled with radionuclides is poured into a confined cavity of the measured industrial part. Then, the positrons emitted by the decay of the tracer nuclide combine with nearby electrons and annihilate to produce

The associate editor coordinating the review of this manuscript and approving it for publication was Utku Kose.
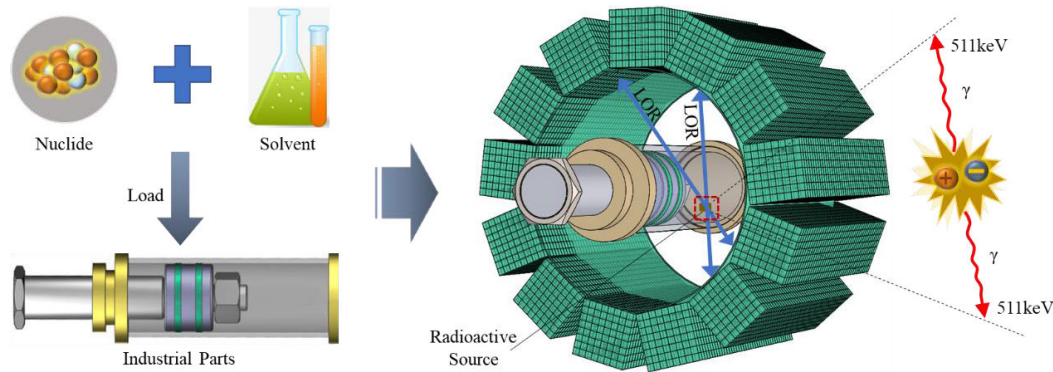
FIGURE 1. Schematic of industrial γ-photon detection and imaging.

γ-photon pairs. A coincidence detection ring is used to capture and record the γ-photon pairs to determine the LORs. Finally, the image of nuclide activity distribution in the inner cavity of the tested industrial part can be restored by a large number of LORs so as to realize the nondestructive detection of the restricted cavity state of the industrial part.

In recent years, the application of γ-photon imaging technology in the industrial field has gradually progressed. In 2015, the Timo team in Germany used the method of single tracer particle detection to detect the density distribution of positrons at a cone angle and then measure the size of the cone angle [5]. In 2016, Liu Jiantang *et al.* successfully tested the defect of an ant nest cavity with γ-photon imaging technology and solved the nondestructive testing of an irregular cavity [6]. In 2017, Yao Min *et al.* successfully used γ-photon imaging technology to image a confined space combustion flow field and observed the state of the combustion field [7]. In 2020, Sun Tong *et al.* proposed a compensatory scattering correction algorithm to improve the quality of reconstructed γ-photon images for the problem of γ-photon scattering caused by high-density industrial metals [8].

With the development of science and technology, γ-photon imaging technology as a precision imaging technology has become a necessity in numerous applications. From small animal research-based PET to large-scale medical PET for the diagnosis of human tissue lesions, the aperture of γ-photon detectors has become increasingly large; for example, the diameter of the Inveon PET [9] detector ring (Siemens, Germany) is 16.1 cm, that of the Discovery PET/CT 710 [10] detector ring (GE, United States) is 81 cm, that of the Biograph mCT PET/CT [11] detector ring (Siemens, Germany) is 84.2 cm, and that of the Gemini TF PET/CT [12] detector ring (Philips, Netherlands) is 90.34 cm. At present, PET systems still image whole spaces. Especially for large aperture PET systems, the image reconstruction process consumes a significant amount of time and computing storage resources.

The materials of industrial parts are mostly composed of high-density alloy and composite materials. On the one hand, when a nuclide solvent is injected into the cavity of an industrial part through perfusion, the high-density alloy material causes significant photon scattering [13], [14], which in turn causes the image to appear in a place with no activity and thus affects image quality. On the other hand, the detection of industrial parts with nuclides requires a certain scanning time. Hence, the nuclide solvent may infiltrate the material during this time and thereby cause blurred edges in the image and even the "expansion" phenomenon. These two issues continue to restrict the application of γ-photon imaging technology in the cavity detection of industrial parts. Hence, a feasible scheme should be developed to achieve the rapid and accurate imaging of the cavities of industrial parts.

In the current work, a ROI imaging algorithm is developed on the basis of the maximum likelihood–expectation maximization (ML-EM) algorithm and the existing point-and-line system matrix (SM) model. Furthermore, imaging resolution is improved by enhancing the existing point-and-line SM model and adding a Gaussian filter in each iteration to suppress the high-frequency noise in images. The feasibility of the algorithm is verified by multigroup simulation experiments and internal cavity detection experiments on hydraulic parts.

II. THEORETICAL BASIS OF γ -PHOTON IMAGE RECONSTRUCTION
A. CONSTRUCTION OF SM
The SM establishes a physical model between the PET detector and the measured object that connects the projection space and the image space. This model is the key to the statistical iterative reconstruction algorithm. Its formula is as follows:

$$Y = A * I \tag{1}$$

where Y is the vectorized sinusoidal image and I is the vectorized tomographic image. A denotes the SM, which establishes the relationship between the sinusoidal graph and the tomographic image. In general, the SM reflects two aspects: the coupling location between a pixel and the LOR, that is, whether the photon emitted by a pixel is detected by the LOR; and the coupling degree between a pixel and the LOR, that is, the probability that the photon emitted by a pixel is detected by the LOR. The quality of the SM affects the quality of the reconstructed image to a great extent.

As shown in Fig. 2, the point-and-line model is widely used as a simple SM construction method. It assumes that the pixel in the image space is an ideal lattice point and that the LOR is an ideal straight line connecting two detector crystals. When calculating the SM, the probability of the photon emitted by the pixel being detected by two LORs is obtained by linear interpolation on the basis of the distance between the pixel and the two adjacent LORs. The total probability of a LOR may also be considered to be 1. If the LOR can interact with N pixels, then the total probability is evenly distributed to N pixels, that is, the probability weight of each pixel is 1/N.
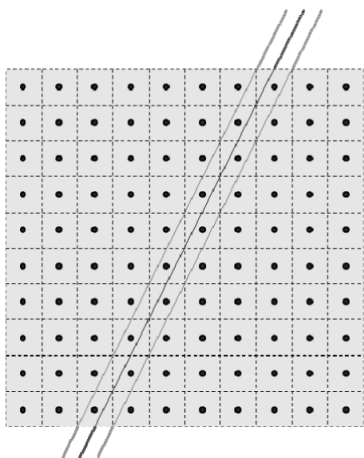

FIGURE 2. Schematic of point-and-line SM model.

B. STATISTICAL ITERATIVE ALGORITHM BASED ON MAXIMUM LIKELIHOOD FUNCTION

The expected value maximization model of the maximum likelihood function is built on the assumption that the emission process of γ photons detected by PET obeys the Poisson distribution [15]. Each pixel value is considered as a parameter to be estimated, and the likelihood function is approximated to the maximum value through continuous iteration and updating so as to obtain the maximum likelihood estimate. According to the principle, the formula of the ML-EM [16], [17] image reconstruction algorithm is as follows:

$$\lambda_j^{k+1} = \frac{\lambda_j^k}{\sum\limits_{i=1}^{I} a_{ij}} \sum_{i=1}^{I} a_{ij} \frac{y_i}{\sum\limits_{t=1}^{J} a_{it}\lambda_t^k} \tag{2}$$

where λ_j^{k+1} is the result of the activity of pixel *j* after the *k+1* iteration, λ_j^{k+1} is the result of the activity of pixel *j* after the *k* iteration, a_{ij} represents the probability that the photon emitted by pixel *j* is detected by the LOR of article *i*, y_i denotes the actual measured value of the LOR of article *i* (current value of the LOR in the sinogram). Eq. (2) comprises three parts, which are presented in Eqs. (3), (4), and (5).

$$c_j = \sum_{i=1}^{I} a_{ij} \tag{3}$$

$$q_i = \sum_{t=1}^{J} a_{it}\lambda_t^k \tag{4}$$

$$b_j = \sum_{i=1}^{M} a_{ij} \frac{y_i}{q_i} \tag{5}$$

The sensitivity correction factor c_j represents the synthesis of the probability that the emitted photons in pixel *j* are detected by any LOR. It gives the sensitivity of each point in the system field of view, which is also known as the normalization factor. q_i represents the contribution of pixels passing through the LOR of article *i* to the projection value of the LOR of article *i*. This process is called orthographic projection, and the corresponding back projection process is represented by b_j. As shown in Eq. (6), the process is an image updating process.

$$\lambda_j^{k+1} = \frac{\lambda_j^k}{c_j} b_j \tag{6}$$

However, the ML-EM algorithm has low data utilization and slow convergence speed. Hence, the OSEM image reconstruction algorithm was proposed by Hudson and Larkin [18] on the basis of the ML-EM. The formula is shown in Eq. (7).

$$\lambda_j^{k+1} = \frac{\lambda_j^k}{\sum\limits_{i \in Sn} a_{ij}} \sum_{i \in Sn} a_{ij} \frac{y_i}{\sum\limits_{t=1}^{J} a_{it}\lambda_t^k} \tag{7}$$

where S_n is the *n* th subset of the total number of events. In this algorithm, the total number of events is divided into *n* subsets according to some method, and the subsets are iterated each time. This approach can improve the data utilization and accelerate the convergence speed. In this work, the total number of events is divided by the angle method.

### C. TOMOGRAPHIC IMAGE RECONSTRUCTION ALGORITHM FOR ROI

In the traditional statistical iterative reconstruction algorithm, image reconstruction is based on the assumption that the annihilation point has equal probability in LOR. Thus, all pixels within a certain length from the LOR should be assigned probability weights. In this case, imaging appears where radioactivity should not exist in the γ-photon image, the intensity of the place for actual imaging is weakened, and the pixel value of the image deviates from the actual value. Moreover, the radioactivity concentration in the active area is reduced, the size of the image increases, the boundary becomes blurred, and the phenomenon of "expansion" occurs. In industrial nondestructive testing, rapid imaging at a low scanning time is required. This requirement tends to lead to the obvious attenuation of image intensity in the activity region along its center toward the periphery. The edge contrast also decreases. As shown in Fig. 3(a), the physical model of Derenzo is commonly used to verify the imaging resolution of PET. Fig. 3(b) shows the image reconstructed by the Derenzo model.
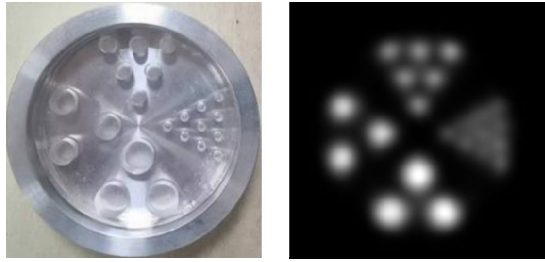
(a) Derenzo physical model   (b) Reconstructed image

FIGURE 3. Derenzo model and its reconstructed tomographic image.

When the industrial equipment is unchanged, that is, the nuclide injection area is unchanged, the imaging resolution decreases if the detector aperture is increased to obtain the ROI reconstruction image of the same size. As shown in Fig. 4, if the same part is installed in a detector system with different apertures, then the ROI of the part to be detected is the same, that is, the nuclide injection area is the same. If the ROI imaging size remains unchanged, then the number of effective pixels for ROI imaging of the large aperture detector system shown in Fig. 4(a) is 4; that of the small aperture detector system shown in Fig. 4(b) is 16, which greatly reduces the ROI imaging resolution.
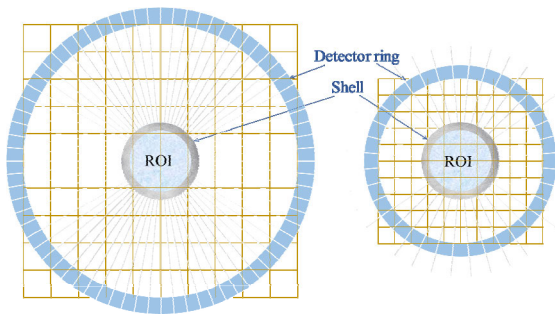
(a) Large aperture detector   (b) Small aperture detector

FIGURE 4. Schematic diagram of large and small aperture detectors with the same parts.

To eliminate the edge effect and improve the imaging resolution, this study proposes an ROI-SM tomographic image reconstruction algorithm. According to prior information about the contour parameters of industrial parts, the SM *A* is improved, and only the pixels in the activity area are given probability weights to form a new SM A_{ROI}. This approach limits the area of positron annihilation to the ROI. From the perspective of probability analysis, annihilation point can be distributed accurately and thereby facilitate the generation of high-resolution images in a large aperture detection system within a short period.

As shown in Fig. 5(a), the traditional method cannot determine the precise position of the annihilation point on the LOR. Thus, the method considers the annihilation point as occurring on all pixels through the LOR with equal probability. Fig. 5(b) shows the schematic of the full pixel allocation for the ROI. According to the known structural parameters of the part, the annihilation point occurs in the pixel of the activity area through which the LOR passes. Therefore, all pixels passed through by the LOR in the activity area are allocated with equal probability, and Eq. (8) is deduced on the basis of Eq. (2).

$$\lambda_j^{k+1} = \frac{\lambda_j^k}{\sum_{i \in Sn, j \in \Omega} a_{ij}^{ROI}} \sum_{i \in Sn} a_{ij}^{ROI} \frac{y_i}{\sum_{t \in \Omega} a_{it}^{ROI} \lambda_t^k} \quad (8)$$

In Eq. (8), a_{ij}^{ROI} denotes the contribution probability of the *i* th LOR to pixel *j*; here, Ω represents the ROI, and the other elements are the same as those defined for Eq. (2). This method can deal with the edge problem of γ-photon imaging caused by permeation and scattering. Moreover, it can quickly and accurately image the internal complex state of industrial parts in the large aperture detection system.

D. OPTIMIZATION OF ALGORITHM

To obtain an accurate and high-quality image, the SM weight in the ROI-based OSEM algorithm is optimized, and the Gaussian filter is used to denoise the results of each iteration according to the characteristics of the γ-photon image. Section B introduces the common point-and-line SM model. In this model, the probability of detection by the same LOR is the same for all pixels that pass through the same LOR. In fact, the probabilities of the concordant detection of pixels located at different positions on the same LOR are quite different. When the pixel size of the point-and-line model is extremely small relative to the LOR, the approximation degree of the point-and-line model will not be considerably large. In most cases, the point-and-line model is too rough, the accuracy is not high, and the reconstruction effect is not ideal. Therefore, the solid angle model is proposed on the basis of the point-and-line model. The solid angle model assumes that the pixel is an ideal grid point and that the line of the crystal bars has a certain cross section. The solid angle of the crystal bar relative to the pixel is taken as the corresponding SM weight. As the two γ photons produced by positron annihilation are not independent of each other, the smaller solid angle is chosen as the coincidence detection probability.

As shown in Fig. 6, point Q is the pixel at the midpoint of the LOR connecting probe crystal A and probe crystal B. The smaller solid angle corresponding to pixel Q is the maximum solid angle of the LOR and is denoted as θ_{max}. Point P is a pixel passed through by the LOR connecting probe crystal A and probe crystal B. The smaller solid angle corresponding to pixel P is denoted as θ. The probability that the photon emitted by pixel P is detected by the LOR is $\frac{\theta}{\theta_{max}}$, and the probability that the photon emitted by pixel Q is detected by the LOR is 1. The high-resolution image reconstruction formula for the ROI based on the solid angle model is shown
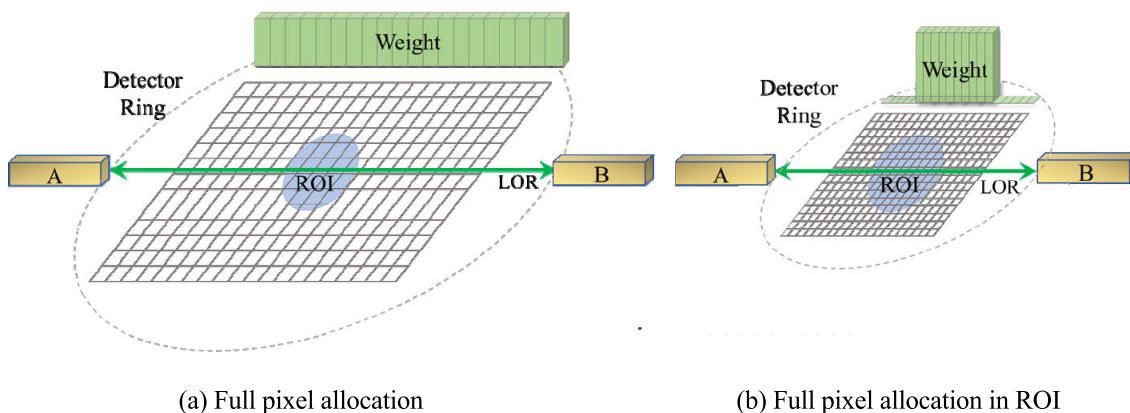
(a) Full pixel allocation   (b) Full pixel allocation in ROI

FIGURE 5. Schematic of weight distribution of LOR.
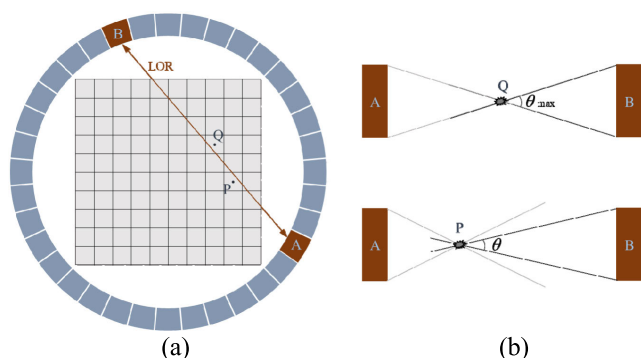

(a)   (b)

FIGURE 6. Schematic of solid angle model.

as follows:

$$\lambda_j^{k+1} = \frac{\lambda_j^k}{\sum_{i \in Sn, j \in \Omega} \left(\frac{\theta_{ij}}{\theta_i \max}\right)} \sum_{i \in Sn} \left(\frac{\theta ij}{\theta_i \max}\right) \frac{y_i}{\sum_{t \in \Omega} \left(\frac{\theta_{it}}{\theta_i \max}\right) \lambda_t^k} \tag{9}$$

In the calculation of the SM, the LOR is actually only related to a small part of the pixels. The same is especially true for the full pixel allocation within the ROI proposed in this work. This condition limits the positron annihilation point to the pixel at the intersection of the LOR and ROI, which only occupies a small part of the whole image. Therefore, the SM has high sparseness, and zero elements do not play a role in the reconstructed projection and back projection. Therefore, a triplet structure is adopted, that is, only the rows, columns, and values of nonzero elements are stored in this compact form. This approach reduces the storage space by about 98% and further improves the reconstruction speed.

III. EXPERIMENTAL VERIFICATION AND ANALYSIS

A. IMAGE EVALUATION INDEX

The mean gradient A, image entropy H, and reconstruction time T are used in this work to evaluate the quality of the reconstructed image and thereby verify the effect of the OSEM reconstruction algorithm for the ROI.

The γ-photon image is divided into two regions: the ROI with activity and the region outside the activity. For the γ-photon image as a discrete two-dimensional function, the gray value is ideally a step change at the ROI contour edge, and the gradient value is large. However, because of scattering and leakage, the image becomes blurred, the gray level of the contour edge can be easily changed, the gradient value is small, and the image contour is not obvious. Therefore, the mean gradient is selected as one of the indicators to measure the γ-photon image. The formula is shown in Eq. (10).

$$A = \frac{\sum_{i=1}^{m-1} \sum_{j=1}^{n-1} \sqrt{\frac{(f(i,j)-f(i+1,j))^2 + (f(i,j)-f(i,j+1))^2}{2}}}{(m-1)(n-1)} \tag{10}$$

In the formula, $f(i,j)$ is the pixel value of row i and column j; m and n are the numbers of rows and columns of the image, respectively. The mean gradient refers to the ability of the image to express the contrast of the tiniest details. The larger the value is, the clearer the image is, and the better the contrast expression ability is.

To further measure the detail gap of γ-photon images, this study proposes another index, that is, image entropy. Image entropy is a statistical form of image features that can reflect the information contained in the aggregation features of the gray distribution in an image. Its formula is shown in Eq. (11).

$$H = \sum_{t=0}^{255} (p_i \log p_i) \tag{11}$$

where t refers to all possible gray values contained in the image with a range of [0,255] and p_i represents the probability of pixel i appearing. Image entropy represents the index of image details. The larger the image entropy is, the greater the image details are, and the better the effect is.

B. RESEARCH ON MODEL EXPERIMENT

Geant4 is a Monte Carlo software package widely used in nuclear physics and particle physics. GATE (Geant4 Application for Tomographic Emission) is a specific application of Geant4 on emission faults [19]–[21]. The GATE simulation of this experiment runs on Ubuntu 16.04. By constructing a geometric model of the trans-PET detector (Table 1), the corresponding simulation parameters are set for the PET simulation.

Two groups of models are used in the experiments to verify the effectiveness of the algorithm. The first is a set of practical experiments, in which a model is used to simulate the convex defect of the actual tee pipe interface. The model is 3D printed with polylactic acid (PLA) material. The second is a group of simulation experiments involving cylinders with different diameters.

As shown in Figs. 7(a)–(b), the pipe has a convex defect, and the inside is the ROI filled with ^{18}F-FDG radionuclide. After the PET test, the 26th reconstructed slice image of the defective tee pipe model is selected for the comparative study. In Fig. 8, the defect with more image features after reconstruction is marked by a red box to observe the difference of different SM imaging clearly. Figs. 8(a)–(d) present the slices reconstructed by the OSEM algorithm using the traditional 100×100 point-and-line model SM, the traditional 200×200 point-and-line SM model, the improved 200×200 solid angle SM model, and the improved 200×200 SM with ROI restriction. Fig. 8(a) shows the slice magnified twice after reconstruction. The data are divided into four subsets and iterated four times. A Gaussian filter is added in the iterative process, and the filter width is fixed at 6 mm. The image in Fig. 8(a) is the most blurry, its edge transition is the smoothest, and the imaging effect is the worst. That in Fig. 8(b) is much less blurry, and the edge is better than that in Fig. 8(a). The image in Fig. 8(c) is relatively clear, and the edge is more enhanced than that in Fig. 8(a). Fig. 8(d), especially the model contour, appears to be clear and has good step characteristics.
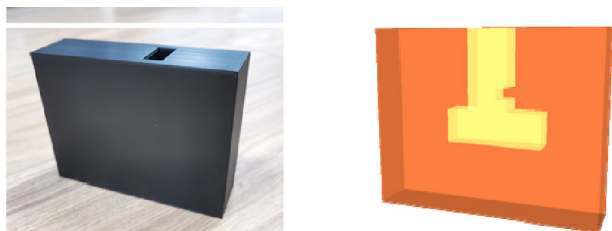
(a) Defective tee pipe model **(b)** Internal structure of defective tee pipe model

FIGURE 7. Schematic of tee pipe model.

Fig. 9 presents a curve showing the variation of reconstruction imaging time of four different SMs with the number of iterations in Fig. 8. The reconstruction algorithms in this work are all run on the MATLAB platform, and the computer is configured with Intel Corporation i5-8300H @ 2.3 GHz
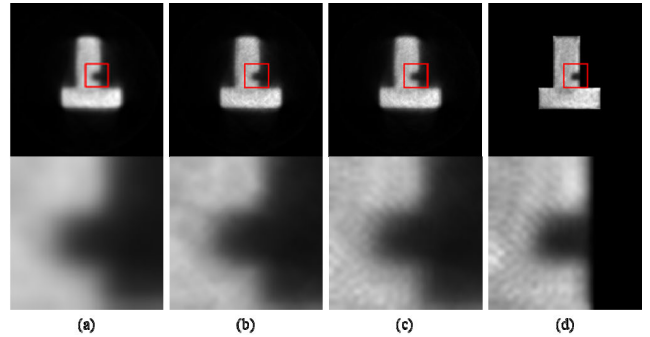

FIGURE 8. Results of four iterations of OSEM: (a) 100×100 point-and-line SM imaging (b) 200×200 point-and-line SM imaging (c) improved 200×200 solid angle SM imaging, (d) improved 200×200 ROI-SM imaging.
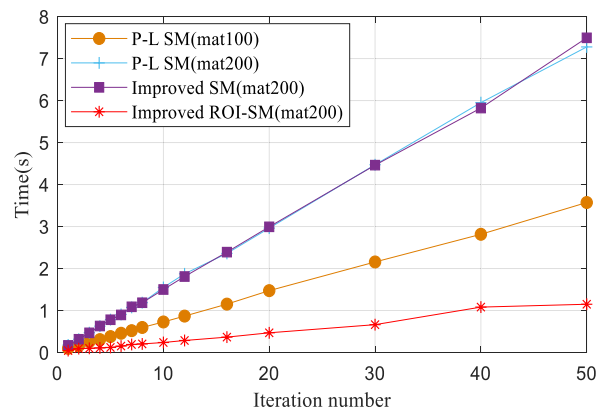

FIGURE 9. Imaging time of each iteration for four types of SM.

quad-core processor. According to Fig. 9, the imaging time of the improved solid angle SM is basically the same as that of the traditional point-and-line SM. Moreover, the imaging time of the improved 200×200 ROI-SM is the shortest and is about six times faster than that of the traditional 200×200 point-and-line SM and even about three times faster than that of the traditional 100×100 traditional point-and-line SM. Hence, the imaging speed of this algorithm is greatly accelerated in the case of improved resolution.

To prove the convergence of this method, this study draws the curves of the mean gradient and image entropy with the number of iterations. The results are shown in Fig. 10. According to the mean gradient curve in Fig. 10, the mean gradient value of the image rises rapidly from the first iteration to the fifth iteration. After the 30th iteration, the mean gradient of the image converges to a fixed value of 1.54. The image entropy change curve shows that the value of image entropy increases obviously in the first 20 iterations, especially in the first 10 iterations. After the 20th iteration, the image entropy converges to a fixed value of 1.23.

The simulation experiment uses a cylinder model to evaluate the improvement effect of the ROI-SM algorithm on edge and clarity. As shown in Fig. 11(c), the gray part of the cylinder model is set as an aluminum alloy shell. The white circular part is the ROI evenly filled with nuclide; its diameter
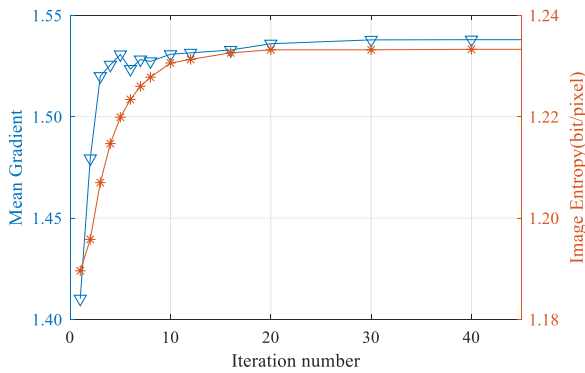
FIGURE 10. Mean gradient and image entropy of each iteration of the algorithm.
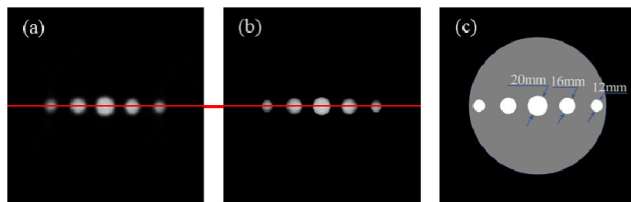

FIGURE 11. Schematic of cylinder model: (a) Slice image reconstruction based on point-and-line SM, (b) slice image reconstruction based on ROI-SM, (c) cylinder model.
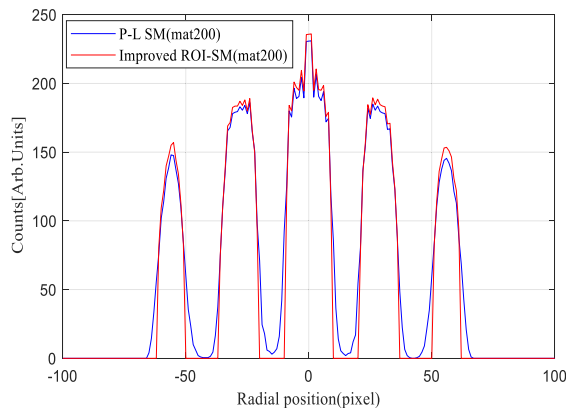

FIGURE 12. Cut view of reconstructions in Fig. 11.

is 12, 16, 20, 16, and 12 mm from left to right, and the center point is the center of symmetry. ^{18}F-FDG radioactive tracer with the same concentration is set in the five horizontal holes. With consideration of the property of rapid detection in industrial applications, the simulation scanning time is set to 30 s, and the point-and-line SM and improved ROI-SM are respectively used to reconstruct the 200×200 high-resolution images. As shown in Figs. 11(a) and (b), the OSEM algorithm is used to iterate for 30 times, and the 26th slice is selected.

As shown in Fig. 12, the differences between the two slice images are compared by drawing into a curve the gray values of the pixels that the red line segment passes through in the reconstructed image. The curve of the image reconstructed based on ROI-SM has the best step performance at the trough

(a) Application of hydraulic parts in aircraft landing gear

(b) Hydraulic part (c) Measuring instrument

FIGURE 13. Application and measuring instrument of hydraulic parts.

and peak value at the crest. Hence, the resolution of the image obtained by this algorithm is relatively high, and the edge performance is particularly prominent.

C. DETECTION EXPERIMENT OF HYDRAULIC PARTS

To verify the feasibility of the proposed algorithm in industrial detection, the research team used the all-digital Trans-PET developed by Suzhou Ruipaining Company of China for the imaging of the inner cavities of hydraulic parts (the parameters are shown in Table 1).

TABLE 1. Characters of Trans-PET.

Parameters	Value
ring number	52
crystals number per ring	312
maximum ring difference	51
projection angles number	156
LORs number per angle	156
radius of detection ring	180 mm
transverse FOV	130 mm
axial FOV	100 mm
crystal size	$1.9 \times 1.9 \times 10$ mm3
crystal pitch	2.0×2.0mm2
time resolution	1.5 ns
FOV central spatial resolution	0.99 mm
average energy resolution	15%
energy window	350-625 keV

Hydraulic technology is based on the Pascal principle and is one of the key technologies to realize modern transmission and control. It has the advantages of large power weight ratio, small volume, small motion inertia, and fast reaction speed. Therefore, hydraulic parts are widely used in many fields. As a result of the high oil pressure in the inner cavity of a hydraulic part, the hydraulic oil easily leaks through the seal or clearance, thereby causing the consumption of hydraulic media and causing environmental pollution. Therefore, the research team tested the inner cavities of hydraulic
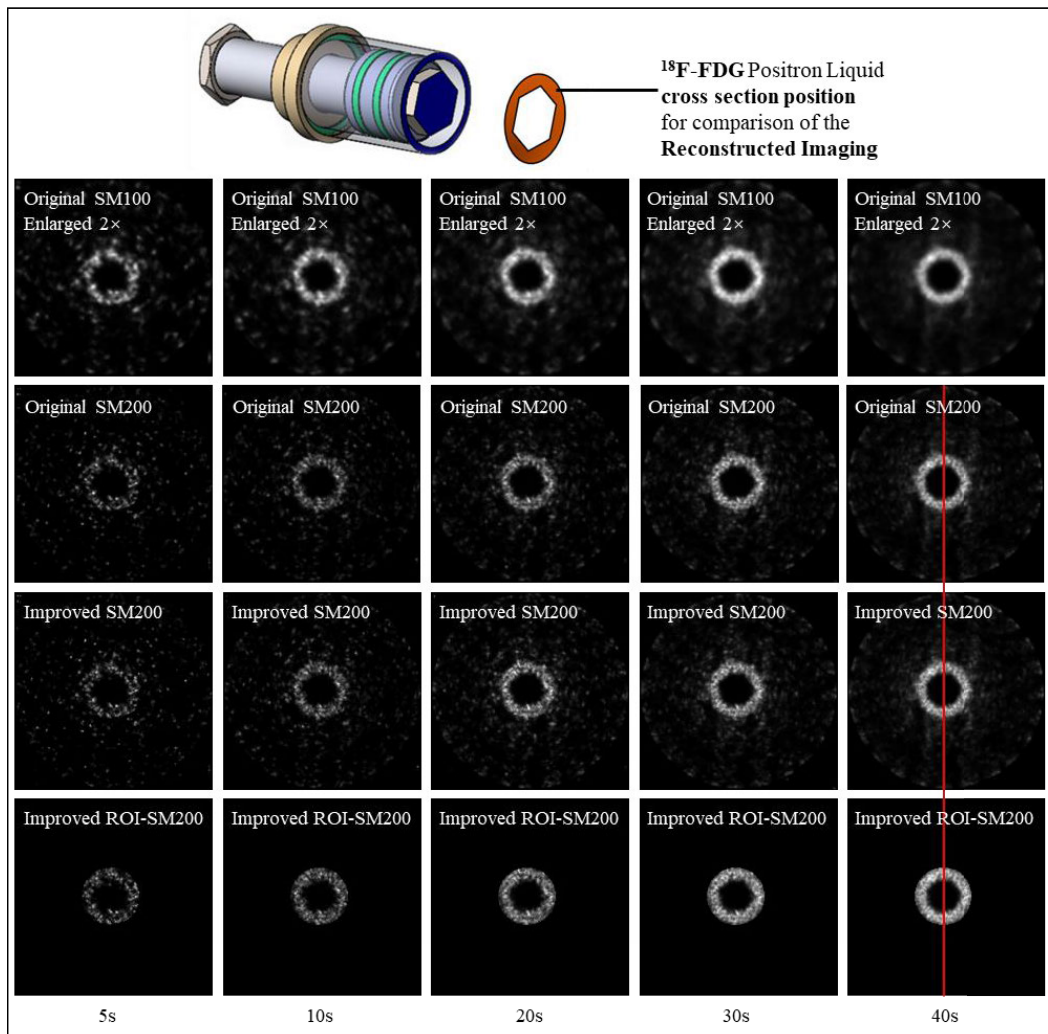
FIGURE 14. Comparison of reconstructed images in different scanning times.

parts. Fig. 13(a) shows the application of hydraulic parts in aircraft landing gear, Fig. 13(b) shows the actual hydraulic parts used in this work, and Fig. 13(c) shows an all-digital trans-PET for testing hydraulic parts.

The wall thickness of the hydraulic part used in the experiment is 5 mm, the outer diameter is 73 mm, and the material is made of stainless steel. The activity of the nuclide injected into the cavity of the hydraulic part is 500 μCi. To study the imaging speed and image improvement effect under different scanning times, this study sets the scanning time of the hydraulic parts to 5, 10, 20, 30, and 40 s. The traditional 100×100 point-and-line SM, the traditional 200×200 point-and-line SM, the improved 200×200 solid angle SM, and the improved 200×200 ROI-SM are used for two-dimensional reconstruction, and the sixth slice image after reconstruction is selected. The slice image reconstructed by the traditional 100×100 point-and-line SM is enlarged twice and is shown in Fig. 14.

Fig. 14 shows the slice images reconstructed by four different SMs. The vertical comparison shows that the image reconstructed by the first line of the traditional 100×100 point-and-line SM is the most blurred. The image reconstructed by the improved solid angle SM in the third line is clearer than that in the second line of the traditional point-and-line SM. The fourth line of the ROI-SM reconstruction image has no noise outside the contour, and the edge improvement is obvious. Moreover, the whole image looks "clean" and relatively clear. To make an objective vertical comparison, this study selects the reconstructed slice image with the best quality and scanning time of 40 s for sectioning in the red line in Fig. 14 (Fig. 15(a)). The image reconstructed by the improved ROI-SM is obviously the highest in both peaks and shows good step performance in the trough, high contrast, and good quality. The image reconstructed by the traditional point-and-line SM is the lowest in the two peaks, that is, it has low contrast and low quality. The results show that the image quality of the improved ROI-SM is satisfactory.

The horizontal comparison shows that with an increase in scanning time, the clarity and brightness of the image increases. To compare the ROI-SM reconstructed images
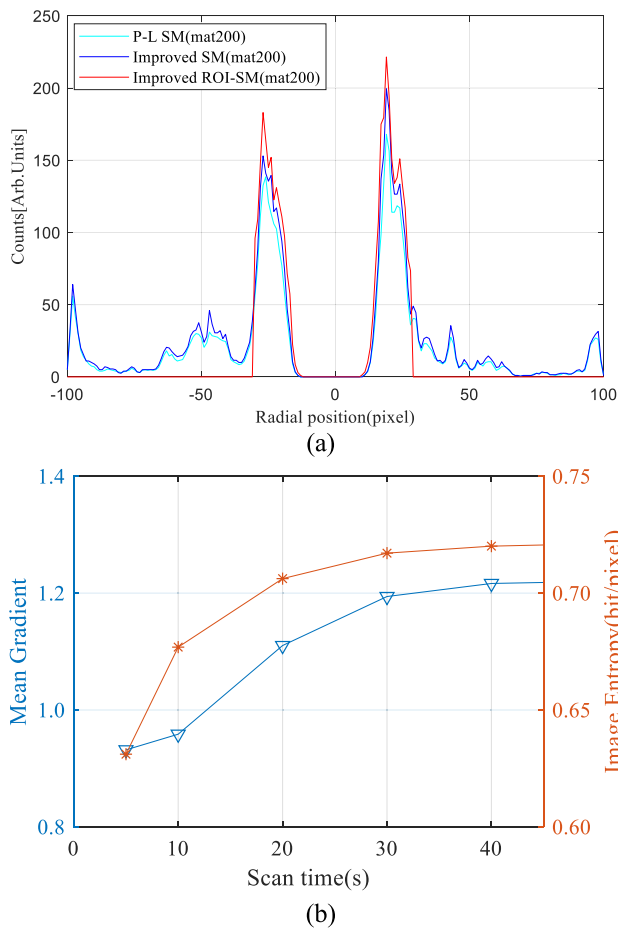
FIGURE 15. (a) Gray value of the image pixel passed by the red line segment in Fig. 14, (b) mean gradient and image entropy of different scanning times of this algorithm.

SM	Reconstruction time (scan time: 5s)	Reconstruction time (scan time: 10s)	Reconstruction time (scan time: 20s)	Reconstruction time (scan time: 30s)	Reconstruction time (scan time: 40s)
P-L SM(100)	2.15s	2.19s	2.19s	2.18s	2.18s
P-L SM(200)	4.43s	4.43s	4.46s	4.46s	4.43s
Improved SM(200)	4.49s	4.49s	4.49s	4.51s	4.49s
Improved ROI-SM(200)	0.41s	0.41s	0.42s	0.41s	0.41s

objectively, we calculate the mean gradient and image entropy of the five images in the fourth line of Fig. 14. As shown in Fig. 15(b), with the increase of scanning time, the mean gradient and the image entropy become large, but the increase drops gradually and tends to be flat. The results show that the longer the scanning time is, the better the image quality reconstructed by the ROI-SM. However, when the scanning time reaches a certain point, the image quality is no longer improved significantly.

To further measure the reconstruction effect of the four types of SM, we statistically analyze the reconstruction time of different SMs along with scanning time. As shown in Table 2, the reconstruction time of the OSEM algorithm is not related to the length of the scanning time, and the reconstruction time of the improved SM is almost the same as that of the traditional point-and-line SM. The reconstruction time of the improved ROI-SM (200) is the shortest, and it is nearly 10 times faster than that of the traditional point-and-line SM (200) with the same size. It is even nearly five times faster than the traditional point-and-line SM (100) with four times less data. This result fully demonstrates the rapidity of the proposed reconstruction algorithm based on the ROI-SM.

IV. CONCLUSION

In this work, an image reconstruction algorithm based on the ROI-SM is proposed for use in γ-photon imaging technology in the industrial field, especially for the cavity detection of industrial parts. The cylinder model and tee pipe model with defects are designed for the simulation experiments, and a field test on the hydraulic parts is conducted. The experimental results show that relative to the traditional point-and-line SM, the improved solid angle model in this work improves the resolution of reconstructed images at the same reconstruction time. Combined with the ROI image reconstruction algorithm, the proposed model improves the image edge obviously, and the reconstruction speed is greatly accelerated. In the simulation experiment, the reconstruction speed is increased by more than six times. Image quality improves with the increase in the number of iterations, and the image quality tends to be stable after 20 iterations. In the test on the hydraulic parts, the imaging speed is increased by more than 10 times, and the image quality is found to improve with the increase of the scanning time. Therefore, the proposed algorithm can also provide a feasible solution for the fast imaging of the details of a large diameter PET detection system.

REFERENCES

[1] D. L. Bailey, M. N. Maisey, D. W. Townsend, and P. E. Valk, *Positron Emission Tomography*, vol. 2. London, U.K.: Springer, 2005.

[2] J. M. Ollinger and J. A. Fessler, "Positron-emission tomography," *IEEE Signal Process. Mag.*, vol. 14, no. 1, pp. 43–55, Jan. 1997, doi: 10.1109/79.560323.

[3] T. F. Budinger and T. Jones, "History of nuclear medicine and molecular imaging," in *Comprehensive Biomedical Physics*. 2014, pp. 1–37.

[4] P. Zanzonico, "Basic sciences of nuclear medicine," *Med. Phys.*, vol. 38, no. 9, pp. 5265–5266, Aug. 2011, doi: 10.1118/1.3626488.

[5] T. Hensler, M. Tupy, T. Strer, T. Pöschel, and K.-E. Wirth, "Positron emission particle tracking in fluidized beds with secondary gas injection," *Powder Technol.*, vol. 279, pp. 113–122, Jul. 2015, doi: 10.1016/j.powtec.2015.04.005.

[6] L. Jiantang, Z. Min, and X. Hui, "A positron injection-based 3D imaging test method for inner cavities in complex parts," *Insight*, vol. 58, no. 11, pp. 617–622, Nov. 2016, doi: 10.1784/insi.2016.58.11.617.

[7] M. Yao, Y. Zhang, M. Zhao, R. Guo, and J. Xu, "Research on combustion flow field imaging method based on ray casting algorithm," *AIP Adv.*, vol. 9, no. 5, May 2019, Art. no. 055022, doi: 10.1063/1.5042043.

[8] M. Zhao, T. Sun, M. Yao, R. Guo, T. Jiang, Z. Zhao, and Y. Li, "A study on compensatory scattering correction of industrial γ-photon 3D imaging method," *AIP Adv.*, vol. 10, no. 7, Jul. 2020, Art. no. 075118, doi: 10.1063/5.0015022.

[9] C. C. Constantinescu and J. Mukherjee, "Performance evaluation of an Inveon PET preclinical scanner," *Phys. Med. Biol.*, vol. 54, no. 9, pp. 2885–2899, May 2009, doi: 10.1088/0031-9155/54/9/020.

[10] H. J. Yoon, Y. J. Jeong, H. J. Son, D.-Y. Kang, K.-Y. Hyun, and M.-K. Lee, "Optimization of the spatial resolution for the GE discovery PET/CT 710 by using NEMA NU 2-2007 standards," *J. Korean Phys. Soc.*, vol. 66, no. 2, pp. 287–294, Jan. 2015, doi: 10.3938/jkps.66.287.

[11] I. Rausch, J. Cal-González, D. Dapra, H. J. Gallowitsch, P. Lind, T. Beyer, and G. Minear, "Performance evaluation of the biograph mCT flow PET/CT system according to the NEMA NU2-2012 standard," *EJNMMI Phys.*, vol. 2, no. 1, p. 26, Dec. 2015, doi: 10.1186/s40658-015-0132-1.

[12] S. Surti, A. Kuhn, M. E. Werner, A. E. Perkins, J. Kolthammer, and J. S. Karp, "Performance of Philips Gemini TF PET/CT scanner with special consideration for its time-of-flight imaging capabilities," *J. Nucl. Med.*, vol. 48, no. 3, pp. 471–480, Mar. 2007.

[13] H. Xiao, M. Zhao, J. Liu, and H. Chen, "A study on scattering correction for γ-photon 3D imaging test method," *AIP Adv.*, vol. 8, no. 3, Mar. 2018, Art. no. 035315, doi: 10.1063/1.5022486.

[14] H. Xiao, M. Zhao, J. Liu, J. Liu, and H. Chen, "A new method for spatial structure detection of complex inner cavities based on 3D γ-photon imaging," *AIP Adv.*, vol. 8, no. 5, May 2018, Art. no. 055205, doi: 10.1063/1.4984027.

[15] G. T. Herman, "Image reconstruction from projections," *Real-Time Imag.*, vol. 1, no. 1, pp. 3–18, Apr. 1995, doi: 10.1006/rtim.1995.1002.

[16] L. A. Shepp and Y. Vardi, "Maximum likelihood reconstruction for emission tomography," *IEEE Trans. Med. Imag.*, vol. MI-1, no. 2, pp. 113–122, Oct. 1982, doi: 10.1109/TMI.1982.4307558.

[17] K. Lange and R. Carson, "EM reconstruction algorithms for emission and transmission tomography," *J. Comput. Assist. Tomogr.*, vol. 8, no. 2, pp. 306–316, Apr. 1984.

[18] H. M. Hudson and R. S. Larkin, "Accelerated image reconstruction using ordered subsets of projection data," *IEEE Trans. Med. Imag.*, vol. 13, no. 4, pp. 601–609, Dec. 1994, doi: 10.1109/42.363108.

[19] S. Jan *et al.*, "GATE: A simulation toolkit for PET and SPECT," *Phys. Med. Biol.*, vol. 49, no. 19, pp. 4543–4561, Oct. 2004, doi: 10.1088/0031-9155/49/19/007.

[20] P. Gonias, N. Bertsekas, N. Karakatsanis, G. Saatsakis, A. Gaitanis, D. Nikolopoulos, G. Loudos, L. Papaspyrou, N. Sakellios, X. Tsantilas, A. Daskalakis, P. Liaparinos, K. Nikita, A. Louizi, D. Cavouras, I. Kandarakis, and G. S. Panayiotakis, "Validation of a GATE model for the simulation of the siemens biograph^{TM} 6 PET scanner," *Nucl. Instrum. Methods Phys. Res. A, Accel. Spectrom. Detect. Assoc. Equip.*, vol. 571, nos. 1–2, pp. 263–266, Feb. 2007, doi: 10.1016/j.nima.2006.10.078.

[21] M. Rodríguez-Villafuerte, Y. Yang, and S. R. Cherry, "A Monte Carlo investigation of the spatial resolution performance of a small-animal PET scanner designed for mouse brain imaging studies," *Phys. Medica*, vol. 30, no. 1, pp. 76–85, Feb. 2014, doi: 10.1016/j.ejmp.2013.03.004.

GANG LV was born in Huaian, Jiangsu, China, in 1997. He received the B.Sc. degree from the Nanjing Institute of Technology, China, in 2019. He is currently pursuing the Graduate degree with the Nanjing University of Aeronautics and Astronautics. His research interests include positron nondestructive testing, algorithm optimization, and high-performance computing.

MIN ZHAO is currently a Professor and a Ph.D. Supervisor with the Nanjing University of Aeronautics and Astronautics. His current research interests include UAV trajectory planning and control, positron annihilation technology for nondestructive testing, computer measurement, and control system for high-speed railway nondestructive testing. He is a member of the Metrology Technology Professional Committee, Chinese Society of Aeronautics and Astronautics, the Vice Chairman of the Thermal Engineering Professional Committee, Jiangsu Institute of Metrology and Testing, and the Chairman of the Supervisory Board, Jiangsu Institute of Instrumentation.

RUIPENG GUO received the Ph.D. degree in instrument science and technology from Shanghai Jiao Tong University, Shanghai, China, in 2011. She is currently an Associate Professor with the Nanjing University of Aeronautics and Astronautics. Her research interests include non-destructive testing, computer measurement, and control and signal processing.

JIAN LIU (Member, IEEE) received the B.S., M.S., and Ph.D. degrees in instrumentation science and technology from the Harbin Institute of Technology (HIT), Harbin, China, in 2005, 2007, and 2011, respectively. He was a joint cultivated Ph.D. student at the Prefectural University of Hiroshima, Hiroshima, Japan, from October 2008 to September 2009. He is currently a Lecturer with the Nanjing University of Aeronautics and Astronautics, Nanjing, China. His main research interests include active noise control, adaptive signal processing, and sensor signal processing. He is a member of the Acoustical Society of China (ASC) and the Institute of Electronics, Information, and Communications Engineers (IEICE) of Japan.

MIN YAO received the B.Sc., M.Sc., and Ph.D. degrees from the Nanjing University of Aeronautics and Astronautics, China, in 1997, 2002, and 2008, respectively. She is currently an Associate Professor with the Nanjing University of Aeronautics and Astronautics. Her research interests include computer measurement, control and UAVs task assignment, data and signal processing, and algorithm optimization.

DAWEI ZHEN was born in Chifeng, Neimenggu, China, in 1997. He received the B.Sc. degree from the Harbin Institute of Technology, China, in 2019. He is currently pursuing the Graduate degree with the Nanjing University of Aeronautics and Astronautics. His research interests include positron nondestructive testing, 3-D display, and computer measurement and control.

MING WANG received the M.Sc. degree from the Harbin University of Science and Technology, in 2020. He is currently pursuing the Ph.D. degree with the Nanjing University of Aeronautics and Astronautics. His main research interests include positron nondestructive testing, algorithm optimization, and 3-D image reconstruction algorithms based on AI.

WEI LIU was born in Fengcheng, Jiangxi, China, in 1995. He received the B.Sc. degree from the Nanjing Institute of Technology, China, in 2019. He is currently pursuing the Graduate degree with the Nanjing University of Aeronautics and Astronautics. His research interests include positron nondestructive testing, algorithm optimization, and data and signal processing.

• • •

FANG XIONG was born in Ganzhou, Jiangxi, China, in 1995. She received the B.Sc. degree from Shandong University, China, in 2018. She is currently pursuing the Graduate degree with the Nanjing University of Aeronautics and Astronautics. Her research interests include positron nondestructive testing, algorithm optimization, and image processing.